

# Grid Strength Assessment Method for Evaluating Small-signal Synchronization Stability of Grid-following and Grid-forming Converters Integrated Systems

Qianhong Shi, *Student Member, IEEE*, Wei Dong, Guanzhong Wang, *Member, IEEE*, Junchao Ma, Chenxu Wang, Xianye Guo, and Vladimir Terzija, *Fellow, IEEE*

**Abstract**—Oscillations caused by small-signal instability have been widely observed in AC grids with grid-following (GFL) and grid-forming (GFM) converters. The generalized short-circuit ratio is commonly used to assess the strength of GFL converters when integrated with weak AC systems at risk of oscillation. This paper provides the grid strength assessment method to evaluate the small-signal synchronization stability of GFL and GFM converters integrated systems. First, the admittance and impedance matrices of the GFL and GFM converters are analyzed to identify the frequency bands associated with negative damping in oscillation modes dominated by heterogeneous synchronization control. Secondly, based on the interaction rules between the short-circuit ratio and the different oscillation modes, an equivalent circuit is proposed to simplify the grid strength assessment through the topological transformation of the AC grid. The risk of sub-synchronization and low-frequency oscillations, influenced by GFL and GFM converters, is then reformulated as a semi-definite programming (SDP) model, incorporating the node admittance matrix and grid-connected device capacities. The effectiveness of the proposed method is demonstrated through a case analysis.

**Index Terms**—Grid-following converter, grid-forming converter, grid strength assessment, small-signal stability.

## I. INTRODUCTION

WITH the large-scale integration of power electronic converters based renewable energy generators into

the AC grid, power system dynamic characteristics have undergone fundamental changes [1], [2], leading to new small-signal instability problems [3]-[5]. For instance, the issues arising from stronger interactions between fast converter controls of power electronic equipment [6], i.e., small-signal instability, are more evident in weak AC grids with high line impedance [7], [8].

Grid strength is a tool for preliminary screening of small-signal stability for converters integrated systems. For instance, the short-circuit ratio (SCR), recently recognized by North American Electric Power Reliability Corporation, has been widely used by power system operators [9]. However, SCR alone is limited to assessing the grid strength of single-converter grid-connected systems and does not address the multi-converter interaction challenges.

Presently, two primary SCR-based methods are utilized to assess the grid strength of the multi-infeed converter systems: heuristic and theoretical derivation-based methods. Heuristic method is derived from indicators inspired by engineering experience, such as the weighted SCR (WSCR) [10] and the multi-infeed SCR (MSCR) [11], which has simple calculation formulas but lacks a theoretical basis. The theoretical derivation-based method is based on the return ratio/difference matrix characteristic analysis, in which the generalized SCR (gSCR) is the mainstream index for assessing the strength of multi-infeed converter systems [12]-[15].

The aforementioned methods primarily focus on analyzing small-signal stability issues in weak grids, such as sub-synchronization oscillation caused by grid-following (GFL) converter equipped with a phase-locked loop (PLL) [6], [13]. To reduce the interaction between PLLs and weak grids, applying grid-forming (GFM) converters has become a research hotspot. The existing control methods of GFM converter can be divided into droop control, virtual synchronous machine (VSM), and matching control [16]-[18]. However, with the increasing integration of GFM converters in the AC grid, instability issues arise in stiff power grids, since the GFM converter without the damping torque provided by the armature reactance of the synchronous generators (SGs) is not as self-stable as the SG in stiff grid [18]. Without loss of generality,

Manuscript received: July 18, 2024; revised: October 25, 2024; accepted: December 5, 2024. Date of CrossCheck: December 5, 2024. Date of online publication: January 30, 2025.

This work was supported by the Science and Technology Project of State Grid Zhejiang Electric Power Co., Ltd. (No. 5211DS24000D).

This article is distributed under the terms of the Creative Commons Attribution 4.0 International License (<http://creativecommons.org/licenses/by/4.0/>).

Q. Shi, G. Wang (corresponding author), and X. Guo are with the Key Laboratory of Power System Intelligent Dispatch and Control of Ministry of Education, School of Electrical Engineering, Shandong University, Jinan 250061, China (e-mail: Sqianhong@163.com; eewgz@sdu.edu.cn; guoxianye.sdu@163.com).

W. Dong, J. Ma, and C. Wang are with the Electric Power Research Institute, State Grid Zhejiang Electric Power Co., Ltd., Hangzhou 310014, China (e-mail: eedongwei@163.com; majunchao1989@gmail.com; Chenxu\_Wang2021@163.com).

V. Terzija is with the School of Engineering, Newcastle University, Newcastle upon Tyne, UK (e-mail: Vladimir.terzija@newcastle.ac.uk).

DOI: 10.35833/MPCE.2024.000759



this paper adopts VSM as a typical GFM control method. Then, contrary to the GFL converter, the GFM converter strongly interacts with the AC grid with a high SCR [19], [20]. Therefore, there is a pressing demand to assess the small-signal stability of hybrid converters integrated systems.

The challenges in small-signal stability assessment of hybrid converters integrated systems stem from the distinctive synchronization control mechanisms of GFL and GFM converters. GFL converters employ PLL to generate the output current phase to achieve reactive power synchronization. In contrast, the GFM converters use virtual synchronization control to generate the output voltage phase to achieve active power synchronization [21]. Due to the coexistence of GFL and GFM converters, the converter synchronization control structure is heterogeneous, the number of converter devices is large, and the spatial locations are dispersed, resulting in a high order of small-signal models and difficulty in risk assessment of hybrid system stability. Additionally, there is a lack of concise assessment indicators for the small-signal stability of hybrid system. Existing research works mainly focus on the capacity evaluation of GFL converters [22]. In [23], the configuration capacity of the GFM converter in the system is evaluated, and it is pointed out that configuring the GFM converter can enhance the stability of the GFL converter-dominated systems.

To tackle the above issues, this paper proposes a grid strength assessment method to evaluate the small-signal synchronization stability of the GFL and GFM converters integrated system (hereafter called the hybrid system). Specifically, the dominant control links and frequency band characteristics of the dominant oscillation modes of the heterogeneous synchronization control are analyzed from the perspective of external characteristics of the converter. An equivalent circuit-based model reduction is then introduced for various oscillation modes. Additionally, a practical renewable energy capacity allocation model based on modified gSCR is proposed. The main contributions of this paper can be summarized as follows:

1) By establishing the admittance and impedance matrices of GFL and GFM converters, the different interaction mechanisms between heterogeneous synchronization control and AC grid are identified from the perspective of external characteristic analysis.

2) Through the interaction rules between SCR and dominant oscillation modes governed by different synchronization controls, an equivalent circuit is proposed, streamlining the grid strength calculation process and facilitating the oscillation risk assessment for hybrid systems.

3) Based on the preceding analysis, a semi-definite programming (SDP) model consisting of a node admittance matrix and grid-connected equipment capacity is proposed. This model serves as a practical tool for planning and operation of hybrid systems to enhance small-signal stability.

The remainder of the paper is organized as follows. Section II analyzes the characteristics of small-signal stability of GFM converters. Section III presents the grid strength of hybrid systems. In Section IV, the modified gSCR application is presented. The simulation results are given in Section

V. Finally, Section VI concludes the paper.

## II. CHARACTERISTIC ANALYSIS OF SMALL-SIGNAL STABILITY OF GFM CONVERTER

Different dynamic external characteristics of GFL converters, GFM converters, and SGs bring differences in the interaction between heterogeneous synchronization control loop and AC grid, e.g., GFL may lose its stability in weak AC grids while GFM may lose its stability in stiff AC grids. To illustrate the reason, this section first analyzes the frequency band of the negative conductance and resistance induced by GFL and GFM converters. Then, by comparing the damping torque of GFM converter and SG, the physical mechanism of low-frequency oscillation of GFM converter in the stiff AC grid is clarified. Finally, the Nyquist criterion is used to analyze the different impacts of grid strength on the dominant oscillation modes of GFL and GFM heterogeneous synchronization control loops.

GFL and GFM converters utilize cascade control structures, comprising outer loops for power and voltage regulations and inner loops for current control. Specifically, the GFL converter employs a constant DC-voltage reactive power control in the outer loop [24], while the GFM converter implements AC voltage control in the outer loop [23]. In addition, since the overcurrent capability of converters is far less than that of SG, the current inner loop is necessary to ensure device safety. However, the distinct external characteristics of these two types of converters are primarily determined by the parameters of their heterogeneous synchronization control. The control structure of a hybrid system is illustrated in Fig. 1, where PWM is short for pulse width modulation;  $PI_{PLL}(s)$  is the PLL transfer function of GFL;  $\omega_0$  is the fundamental frequency of the system;  $D$  and  $J$  are the damping and virtual inertia parameters of the synchronization control loop in the GFM converter, respectively;  $\omega$  and  $\theta$  are the state variables in the synchronization control loop;  $U_g$  is the grid-side voltage (treated as an infinite bus voltage);  $E$  is the output voltage of the converter;  $U$  is the voltage at the point of common coupling (PCC);  $U_{dc}$  is the rated voltage on the DC side;  $I$  and  $I_g$  are the converter output current and the AC grid current, respectively;  $P$ ,  $P_{ref}$ , and  $Q$  are the active power, reference active power, and reactive power, respectively;  $I_{dq}$ ,  $U_{dq}$ ,  $I_{gdq}$ , and  $E_{dq}$  are the components of the variables  $I$ ,  $U$ ,  $I_g$  and  $E$  along the  $dq$ -axis, respectively;  $I_{dref}$  and  $I_{qref}$  are the reference currents along  $d$ - and  $q$ -axis, respectively;  $U_{dref}$  and  $U_{qref}$  are the reference voltages derived from the droop control along  $d$ - and  $q$ -axis, respectively;  $L_f$  and  $C_f$  are the inductance and capacitance of the LC filter, respectively; and  $R_g$  and  $L_g$  are the resistance and inductance of the AC grid, respectively.

### A. Comparison of Frequency Band Characteristics of Negative Damping Between GFL and GFM Converters

The external characteristics of the GFL converter with reactive power synchronization control are similar to those of a current source, making the frequency domain admittance more suitable for small-signal synchronization stability analysis [25].

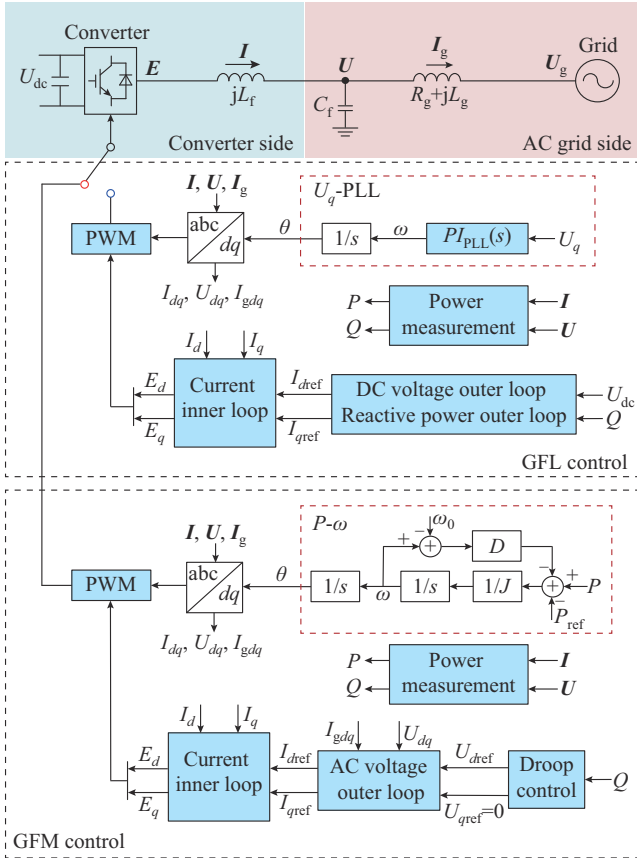


Fig. 1. Control structure of hybrid system.

In contrast, the external characteristics of the GFM converter, which use active power synchronization control, are represented by voltage sources, so the impedance model is typically employed in the small-signal synchronization stability analysis of GFM converter [26]. Therefore, the characteristics of negative conductance and resistance in different frequency bands can be analyzed separately using the Bode diagrams of converter admittance and impedance. The parameters used are given in Tables SAI to SAIII of the Supplementary Material A.

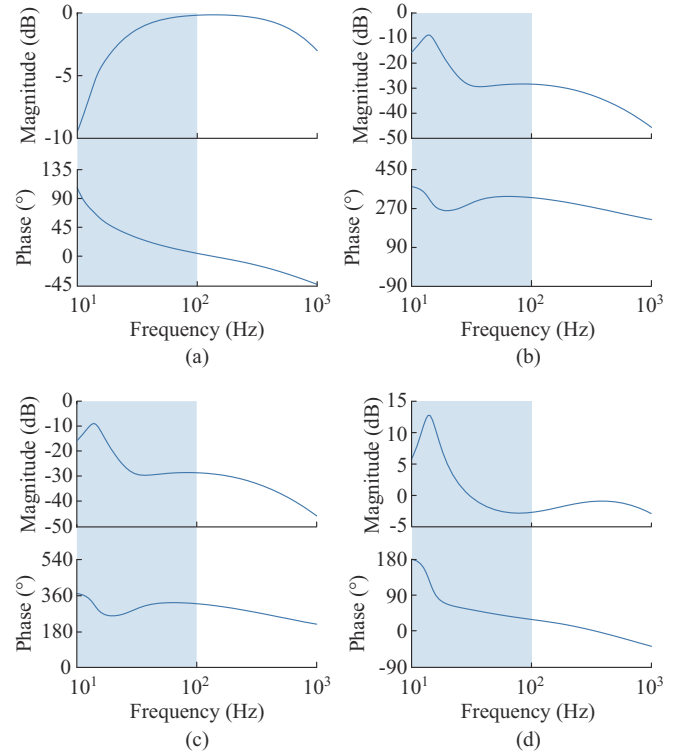
The admittance matrix of the GFL converter can be obtained by:

$$\begin{bmatrix} \Delta I_{gd} \\ \Delta I_{gq} \end{bmatrix} = - \underbrace{\begin{bmatrix} Y_{11}(s) & Y_{12}(s) \\ Y_{21}(s) & Y_{22}(s) \end{bmatrix}}_{\mathbf{Y}_{\text{GFL}}(s)} \begin{bmatrix} \Delta U_d \\ \Delta U_q \end{bmatrix} \quad (1)$$

where  $\Delta$  represents the perturbed value of each of the four variables. The specific element expressions of  $\mathbf{Y}_{\text{GFL}}(s)$  are presented in Supplementary Material A, and the PLL control loop only exists in  $Y_{22}(s)$ . Please refer to [27] and [28] for specific derivation.

The Bode diagram of GFL open-loop system is shown in Fig. 2. As shown in the blue area, in the sub-/super-synchronization oscillation frequency band (10-100 Hz), the magnitude of  $Y_{22}(s)$  is much larger than those of the other three elements, and the phase of  $Y_{22}(s)$  is outside of  $\pm 90^\circ$ . Hence,  $Y_{22}(s)$  provides considerable negative conductance, and  $Y_{22}(s)$  becomes the dominant link in sub-synchronization oscillation.

tion.


 Fig. 2. Bode diagram of GFL open-loop system. (a)  $Y_{11}(s)$ . (b)  $Y_{12}(s)$ . (c)  $Y_{21}(s)$ . (d)  $Y_{22}(s)$ .

For the GFM converter, the impedance matrix can be calculated by [23]:

$$\begin{bmatrix} \Delta U_d \\ \Delta U_q \end{bmatrix} = - \underbrace{\begin{bmatrix} Z_1(s) & 0 \\ Z_2(s) & Z_1(s) \end{bmatrix}}_{\mathbf{Z}_{\text{GFM}}(s)} \begin{bmatrix} \Delta I_{gd} \\ \Delta I_{gq} \end{bmatrix} \quad (2)$$

where  $Z_1(s)$  and  $Z_2(s)$  are the rational transfer functions. The specific element expressions of  $\mathbf{Z}_{\text{GFM}}(s)$  are presented in Supplementary Material A. It is worth noting that the virtual synchronization control loop only appears in  $Z_2(s)$ .

The Bode diagram of GFM open-loop system is shown in Fig. 3. In the low-frequency band (1-10 Hz), the amplitude of  $Z_2(s)$  is much larger than  $Z_1(s)$ , and  $Z_2(s)$  has a more significant negative resistance effect compared with  $Z_1(s)$ . Therefore,  $Z_2(s)$  is the dominant factor in low-frequency oscillation.

To summarize, the analysis of the external characteristics of GFL and GFM converters shows that the heterogeneous synchronization control loop is the primary factor influencing the external characteristics of the converter. In addition, it reveals that the negative damping frequency bands of the two types of converters are distributed in different ranges. As shown in Figs. 2 and 3, the oscillation frequency bands of GFL and GFM converters are staggered. This characteristic is primarily due to the need to set a relatively small control bandwidth for the GFM converter, which is constrained by the limited capacity of the DC-side capacitor.

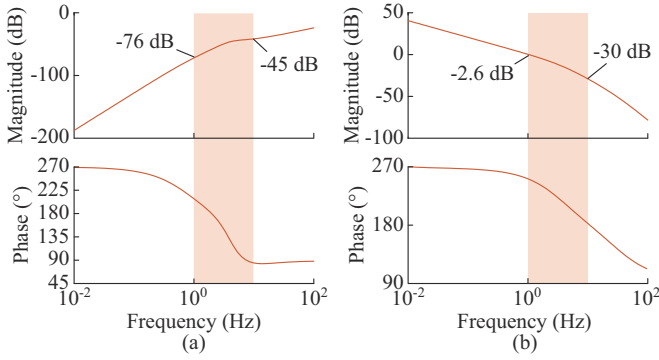


Fig. 3. Bode diagram of GFM open-loop system. (a)  $-Z_1(s)$ . (b)  $-Z_2(s)$ .

### B. Damping Torque Comparison Between GFM Converter and SG

Although both GFM converter and SG have the risk of low-frequency oscillation, the interaction between their oscillation modes and grid strength is different. The armature reactance of SG provides a strong damping torque, and the external grid strength has little effect on its low-frequency oscillation mode. However, the damping torque of the GFM converter is insufficient, and the external grid strength greatly influences the low-frequency oscillation of the GFM converter. Therefore, the influence of grid strength on the GFM converter can be analyzed from the perspective of damping torque. In addition, according to [29], GFM converters using active power synchronization control are susceptible to low-frequency oscillation issues in strong power grids. In contrast, SG also utilizes active power synchronization control, but does not experience this problem in stiff grids.

Hence, the damping torque method will be applied to explain the reasons behind the differences in external characteristics of GFM converters and SGs in the low-frequency range. The contribution of the inner loop of GFM converter and filter inductance is quantitatively evaluated to the damping torque of the synchronization control loop. A theoretical basis will be established to for evaluating the grid strength of hybrid systems.

The SG in this paper adopts the classic 6<sup>th</sup>-order model based on [30], which ignores the fluctuation of the rotor speed. The electromagnetic torque provided by the stator armature circuit can be expressed as [18]:

$$\begin{cases} \Delta T_{SG} \approx \Delta P_e = U_{d0} \Delta I_d + U_{q0} \Delta I_q + I_{d0} \Delta U_d + I_{q0} \Delta U_q = \\ \frac{U_g \sin \delta_0 U_{d0}}{Z_{SGd}(s)} \Delta \delta + \frac{U_g \cos \delta_0 U_{q0}}{Z_{SGq}(s)} \Delta \delta + \frac{K_1 \Delta \delta}{\Delta T_{SG3}} \\ K_1 = U_g (\cos \delta_0 I_{d0} - \sin \delta_0 I_{q0}) \end{cases} \quad (3)$$

where  $\Delta T_{SG}$  is the electromagnetic torque of SG with  $\Delta T_{SG1}$ ,  $\Delta T_{SG2}$ , and  $\Delta T_{SG3}$  as the three components;  $\Delta P_e$  is the electromagnetic power;  $K_1$  is a constant;  $U_g$  is the grid voltage amplitude;  $\delta$  is the power angle;  $Z_{SGd}(s)$  and  $Z_{SGq}(s)$  are the SG impedances in the  $d$ - and  $q$ -axis, respectively; and the subscript 0 represents the steady-state value of the corresponding component, which applies to all subsequent variables.

The vector control loop of the GFM converter is structurally similar to the armature circuit, so its damping torque

$\Delta T_{GFM}$  can be obtained by:

$$\begin{cases} \Delta T_{GFM} \approx \Delta P = U_{d0} \Delta I_d + U_{q0} \Delta I_q + I_{d0} \Delta U_d + I_{q0} \Delta U_q = \\ \frac{U_g \sin \delta_0 U_{d0}}{Z_{GFMd}(s)} \Delta \delta + \frac{U_g \cos \delta_0 U_{q0}}{Z_{GFMq}(s)} \Delta \delta + \frac{K_2 \Delta \delta}{\Delta T_{GFM3}} \\ K_2 = U_g I_{d0} \cos \delta_0 \end{cases} \quad (4)$$

where  $\Delta P$  is the active power perturbed value of GFM converter;  $\Delta T_{GFM}$  is the electromagnetic torque of GFM converter with  $\Delta T_{GFM1}$ ,  $\Delta T_{GFM2}$ , and  $\Delta T_{GFM3}$  as three components;  $K_2$  is a constant; and  $Z_{GFMd}(s)$  and  $Z_{GFMq}(s)$  are the GFM impedances in the  $d$ - and  $q$ -axis, respectively. The derivation process is shown in Supplementary Material B.

The armature reactance of SG and the vector control loop of GFM converter are reflected in  $Z_{SGd,q}(s)$  and  $Z_{GFMd,q}(s)$ . The impedance characteristics of SG and GFM converter are shown in Fig. 4. As shown in the green area, the armature reactance provides positive damping in both the low-frequency band and the sub-synchronization frequency band because the phase lags in  $Z_{SGd,q}(s)$ . In contrast, as shown in the orange area, the current inner loop mainly provides negative damping in the low-frequency band because the phases of  $Z_{GFMd,q}(s)$  are both larger than  $0^\circ$ .

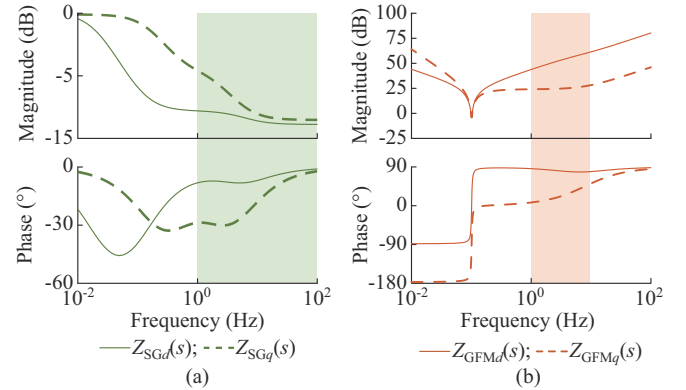


Fig. 4. Impedance characteristics of SG and GFM converter. (a)  $Z_{SGd}(s)$  and  $Z_{SGq}(s)$ . (b)  $Z_{GFMd}(s)$  and  $Z_{GFMq}(s)$ .

At a specific oscillation frequency (assuming  $s = j2$  Hz), the damping torques of SG and GFM converter are illustrated in Fig. 5.

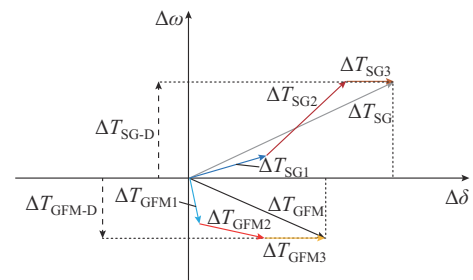


Fig. 5. Damping torques of SG and GFM converter.

Among them,  $\Delta T_{SG1}$  and  $\Delta T_{SG2}$  are positive damping torques (with  $\Delta T_{SG-D}$  as the positive damping component), while the phases of  $\Delta T_{GFM1}$  and  $\Delta T_{GFM2}$  lag behind  $\Delta \delta$ , result-

ing in a negative damping torque component in  $\Delta T_{\text{GFM}}$  (as indicated by  $\Delta T_{\text{GFM-D}}$ ). These results indicate that the armature reactance offers sufficient dynamic damping for SG in a stiff grid, making it less susceptible to low-frequency oscillation. However, the GFM converter with active power synchronization control is prone to low-frequency oscillations.

### C. Comparison of Small-signal Stability Between GFM and GFL Converters in Stiff and Weak Grids

This subsection examines how grid strength interacts with various oscillation modes, offering a theoretical foundation for assessing small-signal stability across different frequency bands. SCR is a vital indicator for measuring the grid strength. It is defined as the ratio of the short-circuit capacity at the infeed bus in a single-infeed system to the rated capacity  $S_B$  of the converter as [31]:

$$SCR = \frac{1}{S_B Z} = \frac{B}{S_B} \quad (5)$$

where  $Z=1/B$  is the reactance connecting the converter with the AC grid, and  $B$  is the susceptance.

The admittance matrix of the single GFL converter integrated system  $Y(s)$  can be represented by the return-difference matrix (RDM) of the system, as shown in (6).

$$Y(s) = Y_{\text{GFL}}(s) + Y_{\text{grid}}(s) \triangleq \begin{bmatrix} Y_A(s) & Y_B(s) \\ Y_C(s) & Y_D(s) \end{bmatrix} \quad (6)$$

where  $Y_{\text{grid}}(s)$  is the admittance matrix of the AC grid. The specific elements  $Y_A(s)$ ,  $Y_B(s)$ ,  $Y_C(s)$ ,  $Y_D(s)$ , and  $Y_{\text{grid}}(s)$  are given as:

$$\begin{cases} Y_A(s) = Y_1(s) + s/L_g(s^2 + \omega_0^2) \\ Y_B(s) = \omega_0/L_g(s^2 + \omega_0^2) \\ Y_C(s) = -\omega_0/L_g(s^2 + \omega_0^2) \\ Y_D(s) = Y_2(s) + s/L_g(s^2 + \omega_0^2) \\ Y_{\text{grid}}(s) = \underbrace{\begin{bmatrix} \frac{s\omega_0}{s^2 + \omega_0^2} & \frac{\omega_0^2}{s^2 + \omega_0^2} \\ \frac{-\omega_0^2}{s^2 + \omega_0^2} & \frac{s\omega_0}{s^2 + \omega_0^2} \end{bmatrix}}_{y(s)} \otimes B \end{cases} \quad (7)$$

As for the GFM converter, the RDM of the single GFM converter integrated system can be obtained by:

$$Z(s) = Z_{\text{GFM}}(s) + Z_{\text{grid}}(s) \triangleq \begin{bmatrix} Z_A(s) & Z_B(s) \\ Z_C(s) & Z_D(s) \end{bmatrix} \quad (8)$$

where  $Z(s)$  is the impedance matrix of the single GFM converter integrated system; and  $Z_{\text{grid}}(s)$  is the AC grid impedance. The specific elements  $Z_A(s)$ ,  $Z_B(s)$ ,  $Z_C(s)$ ,  $Z_D(s)$ , and  $Z_{\text{grid}}(s)$  are given as:

$$\begin{cases} Z_A(s) = Z_1(s) + sL_g \\ Z_B(s) = -\omega_0 L_g \\ Z_C(s) = Z_1(s) + \omega_0 L_g \\ Z_D(s) = Z_1(s) + sL_g \\ Z_{\text{grid}}(s) = \underbrace{\begin{bmatrix} s & -\omega_0 \\ \omega_0 & s \end{bmatrix}}_{z(s)} \otimes B^{-1} \end{cases} \quad (9)$$

The Nyquist criterion is adopted to analyze the small-signal stability between GFM and GFL converters in stiff and weak grids. Specifically, the Nyquist curves of the PLL dominated control loop  $-Y_D(s)/(Y_B(s)Y_A^{-1}(s)Y_C(s))$  of the GFL converter under different grid strengths are shown in Fig. 6(a) and (b), while the Nyquist curves of the virtual synchronization dominated control loop  $-Z_C(s)/(Z_B(s)Z_A^{-1}(s)Z_D(s))$  under SCR changes are shown in Fig. 6(c) and (d). In Fig. 6, + denotes the point  $(-1, j0)$ . The rationality proof of the dominated control loops can be found in Supplementary Material C. The results reveal that the GFL converter has stronger stability in stiff grid, whereas the GFM converter has stronger stability in weak AC grid.

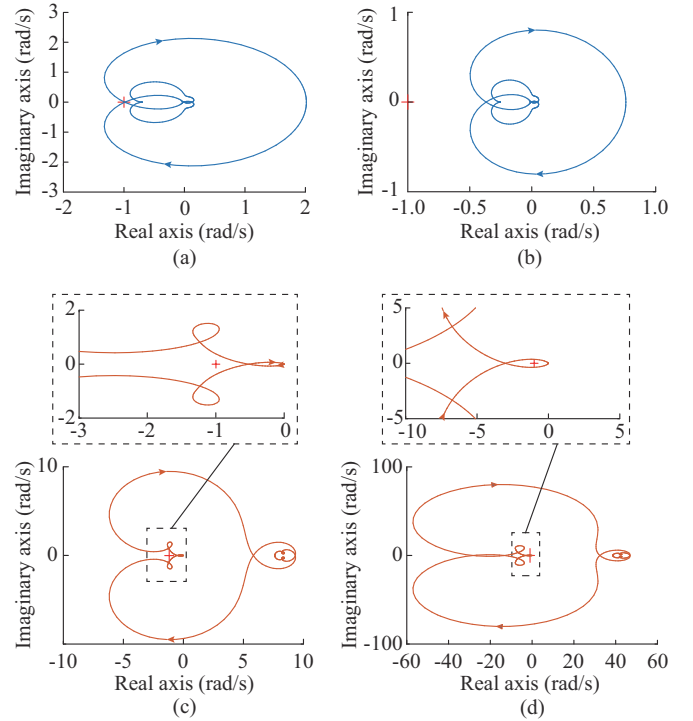


Fig. 6. Nyquist curves of GFL and GFM converters under different grid strength. (a) PLL dominated control loop ( $SCR=1.2$ ). (b) PLL dominated control loop ( $SCR=2$ ). (c) Virtual synchronization dominated control loop ( $SCR=2$ ). (d) Virtual synchronization dominated control loop ( $SCR=8$ ).

### III. GRID STRENGTH CALCULATION OF HYBRID SYSTEM

Due to the small capacity of a single converter based on the renewable energy, the grid-connected structure is characterized by scale and decentralization. In addition, the converter has multi-scale control interactions, so its dynamic model order is also high. The above characteristics make simple and intuitive grid strength indicators such as the gSCR widely used in the preliminary stability screening of multi-infeed converter systems.

#### A. Modeling of Hybrid System

The hybrid system topology is shown in Fig. 7(a). The system contains  $m$  GFL converter nodes,  $n$  GFM converter nodes, and an infinite power node. Figure 7(b) is a schematic diagram of the reduced-order hybrid system topology with equivalent external grid.

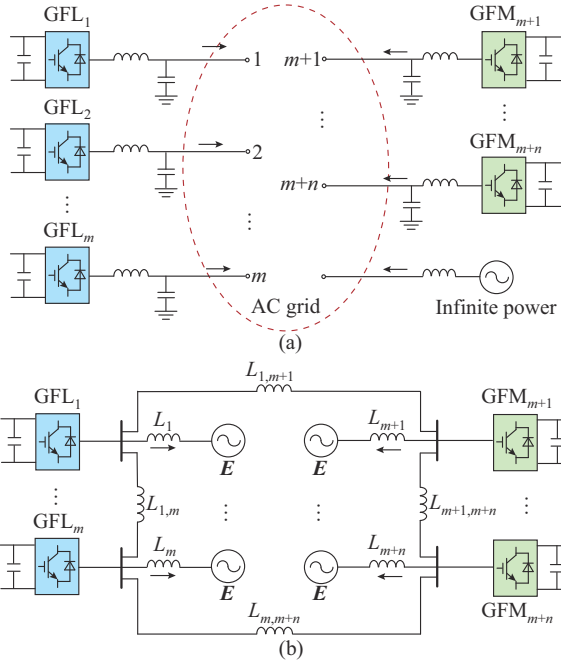


Fig. 7. Hybrid system topology and reduced-order hybrid system topology with equivalent external grid. (a) Hybrid system topology. (b) Reduced-order hybrid system topology with equivalent external grid.

Based on the analysis in Section II,  $\mathbf{Y}_{\text{hybrid}}(s)$  and  $\mathbf{Z}_{\text{hybrid}}(s)$  represent the admittance and impedance of the hybrid system on the converter side, respectively as:

$$\begin{bmatrix} \Delta \mathbf{I} \\ \mathbf{I} \Delta \varphi \end{bmatrix} = - \underbrace{\begin{bmatrix} \mathbf{Y}_{\text{GFL},i}(s) & \mathbf{0} \\ \mathbf{0} & \mathbf{Y}_{\text{GFM},j}(s) \end{bmatrix}}_{\mathbf{Y}_{\text{hybrid}}(s)} \begin{bmatrix} \Delta \mathbf{U} \\ \mathbf{U} \Delta \theta \end{bmatrix} \quad (10)$$

$$\begin{bmatrix} \Delta \mathbf{U} \\ \mathbf{U} \Delta \theta \end{bmatrix} = - \underbrace{\begin{bmatrix} \mathbf{Z}_{\text{GFL},i}(s) & \mathbf{0} \\ \mathbf{0} & \mathbf{Z}_{\text{GFM},j}(s) \end{bmatrix}}_{\mathbf{Z}_{\text{hybrid}}(s)} \begin{bmatrix} \Delta \mathbf{I} \\ \mathbf{I} \Delta \varphi \end{bmatrix} \quad (11)$$

where  $\mathbf{Y}_{\text{GFL},i}(s)$  ( $i=1, 2, \dots, m$ ) and  $\mathbf{Y}_{\text{GFM},j}(s)$  ( $j=m+1, m+2, \dots, n$ ) are the GFL and GFM converter admittance matrices, respectively; and  $\mathbf{Z}_{\text{GFL},i}(s)$  ( $i=1, 2, \dots, m$ ) and  $\mathbf{Z}_{\text{GFM},j}(s)$  ( $j=m+1, m+2, \dots, n$ ) are the GFL and GFM converter impedance matrices, respectively.

The AC grid side admittance and impedance matrices for a multi-infeed converter system, represented by  $\mathbf{Y}_m(s)$  and  $\mathbf{Z}_m(s)$ , expands the matrix from a single-infeed converter system.

$$\begin{cases} \mathbf{Y}_m(s) = \mathbf{B}_{\text{multi}} \otimes \mathbf{y}(s) \\ \mathbf{Z}_m(s) = \mathbf{Z}_{\text{multi}} \otimes \mathbf{z}(s) \end{cases} \quad (12a)$$

$$\left\{ \begin{array}{l} \mathbf{B}_{\text{multi}} = \begin{bmatrix} B_{1,1} & \cdots & B_{1,m} & \cdots & B_{1,m+n} \\ \vdots & \vdots & \vdots & \vdots & \vdots \\ B_{m,1} & \cdots & B_{m,m} & \cdots & B_{m,m+n} \\ \vdots & \vdots & \vdots & \vdots & \vdots \\ B_{m+n,1} & \cdots & B_{m+n,m} & \cdots & B_{m+n,m+n} \end{bmatrix} = \begin{bmatrix} \mathbf{B}_{11} & \mathbf{B}_{12} \\ \mathbf{B}_{21} & \mathbf{B}_{22} \end{bmatrix} \\ \mathbf{Z}_{\text{multi}} = \mathbf{B}_{\text{multi}}^{-1} = \begin{bmatrix} \mathbf{Z}_{11} & \mathbf{Z}_{12} \\ \mathbf{Z}_{21} & \mathbf{Z}_{22} \end{bmatrix} \end{array} \right. \quad (12b)$$

where  $\mathbf{B}_{\text{multi}}$  and  $\mathbf{Z}_{\text{multi}}$  are the node admittance and impedance matrices of the AC grid, respectively;  $\mathbf{B}_{11} \in \mathbb{R}^{m \times m}$ ,  $\mathbf{B}_{12} \in \mathbb{R}^{m \times n}$ ,  $\mathbf{B}_{21} \in \mathbb{R}^{n \times m}$ ,  $\mathbf{B}_{22} \in \mathbb{R}^{n \times n}$ ,  $\mathbf{Z}_{11} \in \mathbb{R}^{m \times m}$ ,  $\mathbf{Z}_{12} \in \mathbb{R}^{m \times n}$ ,  $\mathbf{Z}_{21} \in \mathbb{R}^{n \times m}$ ; and  $\mathbf{Z}_{22} \in \mathbb{R}^{n \times n}$ .

Considering (10) and (12), the closed-loop admittance and impedance matrices of the hybrid system, i.e.,  $\mathbf{Y}_{\text{sys}}(s)$  and  $\mathbf{Z}_{\text{sys}}(s)$ , can be obtained by:

$$\begin{cases} \mathbf{Y}_{\text{sys}}(s) = \mathbf{Y}_{\text{hybrid}}(s) + \mathbf{Y}_m(s) \\ \mathbf{Z}_{\text{sys}}(s) = \mathbf{Z}_{\text{hybrid}}(s) + \mathbf{Z}_m(s) \end{cases} \quad (13)$$

### B. Analysis of Influence of GFM Converter on Oscillation Mode Dominated by GFL Converter

When analyzing the oscillation mode dominated by GFL converter, the admittance model of  $\mathbf{Y}_{\text{sys}}(s)$  can be obtained by:

$$\begin{aligned} \mathbf{Y}_{\text{sys}}(s) &= \begin{bmatrix} \mathbf{Y}_{\text{GFL},i}(s) & \mathbf{0} \\ \mathbf{0} & \mathbf{Y}_{\text{GFM},j}(s) \end{bmatrix} + \begin{bmatrix} \mathbf{B}_{11} & \mathbf{B}_{12} \\ \mathbf{B}_{21} & \mathbf{B}_{22} \end{bmatrix} \otimes \mathbf{y}(s) = \\ & \begin{bmatrix} \mathbf{Y}_{\text{GFL},i}(s) + \mathbf{B}_{11} \otimes \mathbf{y}(s) & \mathbf{B}_{12} \otimes \mathbf{y}(s) \\ \mathbf{B}_{21} \otimes \mathbf{y}(s) & \mathbf{Y}_{\text{GFM},j}(s) + \mathbf{B}_{22} \otimes \mathbf{y}(s) \end{bmatrix} \triangleq \\ & \begin{bmatrix} \mathbf{Y}'_A(s) & \mathbf{Y}'_B(s) \\ \mathbf{Y}'_C(s) & \mathbf{Y}'_D(s) \end{bmatrix} \end{aligned} \quad (14)$$

As can be observed from Section II-A, in the sub-synchronization oscillation frequency band, the external characteristic of GFM converter is a voltage source with small impedance and large admittance. When  $\mathbf{Y}_{\text{GFM},j}(s)$  is very large,  $\Delta \mathbf{Y}(s)$  is very small after taking the  $\mathbf{Y}_{\text{GFM},j}(s)$  inverse in (16). Hence, the reduced-order model in oscillation mode dominated by GFL converter can be obtained by retaining  $\mathbf{Y}_{\text{GFL},i}(s)$  in (14) and converting the remaining parts into  $\mathbf{Y}_{\text{GFL},i}(s)$  via Schur complement transformation:

$$\begin{aligned} \mathbf{Y}_{\text{Schur}}(s) &= \mathbf{Y}'_A - \mathbf{Y}'_B (\mathbf{Y}'_D)^{-1} \mathbf{Y}'_C = \mathbf{Y}_{\text{GFL},i}(s) + \mathbf{B}_{11} \otimes \mathbf{y}(s) - \\ & (\mathbf{B}_{12} \otimes \mathbf{y}(s)) (\mathbf{Y}_{\text{GFM},j}(s) + \mathbf{B}_{22} \otimes \mathbf{y}(s))^{-1} (\mathbf{B}_{21} \otimes \mathbf{y}(s)) \end{aligned} \quad (15)$$

The feasibility of the above model reduction is based on the fact that GFM converter has little effect on the oscillation mode dominated by GFL converter, and the effect of GFM converter can be quantitatively analyzed by perturbation analysis. Hence, the part of (15) containing the GFM converter is defined as the perturbation:

$$\begin{aligned} \Delta \mathbf{Y}(s) &= \mathbf{Y}_{\text{Schur}}(s) - \mathbf{Y}'_A(s) = -(\mathbf{B}_{12} \otimes \mathbf{y}(s)) (\mathbf{Y}_{\text{GFM},j}(s) + \\ & \mathbf{B}_{22} \otimes \mathbf{y}(s))^{-1} (\mathbf{B}_{21} \otimes \mathbf{y}(s)) \end{aligned} \quad (16)$$

In order to verify the rationality of the reduction, the perturbation calculation is performed through the double-infeed system topology of GFL and GFM converters, as shown in Fig. 8.

### C. Analysis of Influence of GFL Converter on Oscillation Mode Dominated by GFM Converter

Similar to (14), when analyzing the oscillation mode dominated by GFM converter, the impedance model of  $\mathbf{Z}_{\text{sys}}(s)$  can be obtained by:

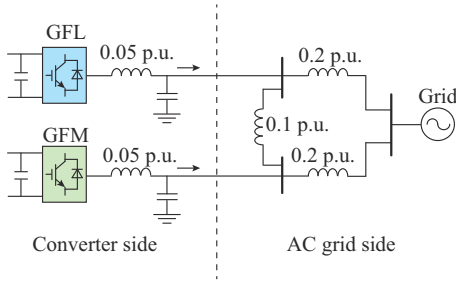


Fig. 8. Double-infeed system topology of GFL and GFM converters.

$$\mathbf{Z}_{\text{sys}}(s) = \begin{bmatrix} \mathbf{Z}_{\text{GFL},i}(s) & \mathbf{0} \\ \mathbf{0} & \mathbf{Z}_{\text{GFM},j}(s) \end{bmatrix} + \begin{bmatrix} \mathbf{Z}_{11} & \mathbf{Z}_{12} \\ \mathbf{Z}_{21} & \mathbf{Z}_{22} \end{bmatrix} \otimes \mathbf{z}(s) = \begin{bmatrix} \mathbf{Z}_{\text{GFL},i}(s) + \mathbf{Z}_{11} \otimes \mathbf{z}(s) & \mathbf{Z}_{12} \otimes \mathbf{z}(s) \\ \mathbf{Z}_{21} \otimes \mathbf{z}(s) & \mathbf{Z}_{\text{GFM},j}(s) + \mathbf{Z}_{22} \otimes \mathbf{z}(s) \end{bmatrix} \triangleq \begin{bmatrix} \mathbf{Z}'_{\text{A}}(s) & \mathbf{Z}'_{\text{B}}(s) \\ \mathbf{Z}'_{\text{C}}(s) & \mathbf{Z}'_{\text{D}}(s) \end{bmatrix} \quad (17)$$

As for the low-frequency oscillation frequency band, the external characteristic of GFL converter is a current source with large impedance and small admittance.  $\mathbf{Z}_{\text{GFM},j}(s)$  can be retained, and the other parts can be converted to  $\mathbf{Z}_{\text{GFM},j}(s)$  through Schur complement transformation to obtain the reduced-order model:

$$\mathbf{Z}_{\text{Schur}}(s) = \mathbf{Z}_{\text{GFM},j}(s) + \mathbf{Z}_{22} \otimes \mathbf{z}(s) - (\mathbf{Z}_{12} \otimes \mathbf{z}(s))(\mathbf{Z}_{\text{GFL},i}(s) + \mathbf{Z}_{11} \otimes \mathbf{z}(s))^{-1} (\mathbf{Z}_{21} \otimes \mathbf{z}(s)) \quad (18)$$

In addition, by making a difference between the matrix  $\mathbf{Z}'_{\text{D}}(s)$  containing the GFM converter admittance  $\mathbf{Z}_{\text{GFM},j}(s)$  in  $\mathbf{Z}_{\text{sys}}(s)$  and the reduced-order model (18), the perturbation quantity of the virtual synchronization dominant oscillation mode can be obtained by:

$$\Delta \mathbf{Z}(s) = (\mathbf{Z}_{\text{Schur}}(s) - \mathbf{Z}'_{\text{D}}(s))(\mathbf{I} \otimes \mathbf{z}(s))^{-2} = -(\mathbf{Z}_{12} \otimes \mathbf{I})(\mathbf{Z}_{\text{GFL},i}(s) + \mathbf{Z}_{11} \otimes \mathbf{z}(s))^{-1} (\mathbf{Z}_{21} \otimes \mathbf{I}) \quad (19)$$

where  $\mathbf{I}$  is the identity matrix of the corresponding dimension.

Furthermore, the singular values of  $\Delta \mathbf{Y}(s)/\Delta \mathbf{Z}(s)$  of the double-infeed system of GFL and GFM converters are analyzed, and the results are shown in Fig. 9. As can be observed from Fig. 9(a), except for the peak near 50 Hz, the maximum singular values of  $\Delta \mathbf{Y}(s)$  are all less than  $-30$  dB in the sub-/super-synchronization frequency band (indicated by the blue area). As shown in Fig. 9(b), the orange area represents the low-frequency band (0-10 Hz), where the maximum singular values of  $\Delta \mathbf{Z}(s)$  are consistently less than  $-30$  dB.

Therefore, the Schur complement transformation has no noticeable effect on the system, proving that the GFM converter has little effect on the oscillation mode dominated by GFL converter and vice versa, further proving that the reduced-order model proposed in this paper is feasible.

On top of that, the critical SCR (CSCR) of the double-infeed system of GFL and GFM converters is close to that of the single-infeed system, further illustrating the effectiveness of the above perturbation analysis. By adjusting the network parameters of the AC power grid, we determine the CSCR

of the double-infeed system in different dominant oscillation modes. Then, by comparing the dominant eigenvalues of the single-infeed system and the double-infeed system under different CSCRs, it is found that when the double-infeed system operates in a weak AC grid, the dominant eigenvalues of the double-infeed system and the single-GFL system are similar. Similarly, the dominant eigenvalues of the double-infeed system and the single-GFM system are similar in a stiff power grid. Detailed eigenvalue results are provided in Table I, where  $B_{11}$ ,  $B_{12}$ ,  $B_{21}$ ,  $B_{22}$  are the four elements of node admittance matrix of the double-infeed system.

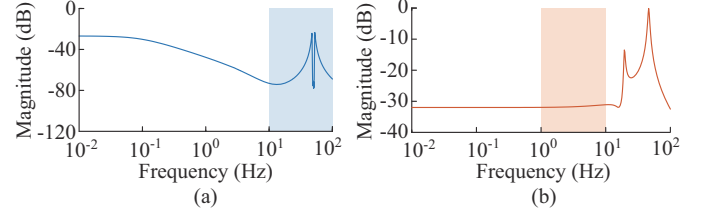


Fig. 9. Frequency response characteristic curve of perturbation quantity in different dominant oscillation modes. (a) PLL dominant oscillation mode. (b) Virtual synchronization dominant oscillation mode.

 TABLE I  
COMPARISON OF EIGENVALUES VALUES

Parameter	System	Eigenvalue
$SCR = 1.73, B_{11} = 1.73$	Double-infeed	$-0.04950 + j66.50$
	Single-GFL	$-0.00653 + j66.30$
$SCR = 11.5, Z_{22} = (B_{22} - B_{21}B_{11}^{-1}B_{12})^{-1} = 0.87$	Double-infeed	$-0.03120 + j9.18$
	Single-GFM	$-0.03070 + j9.23$

In addition, the equivalent circuit topology of a hybrid system corresponds to the system simplification process in different dominant oscillation modes.

In the oscillation mode dominated by GFL converter, the model order reduction can be regarded as treating the GFM converter as an infinite power source, as shown in Fig. 10 (a). Conversely, in the oscillation mode dominated by the GFM converter, the order reduction process can be regarded as treating the GFL converter as an infinite resistor, as shown in Fig. 10(b). For low-frequency oscillation mode, the AC grid side impedance retains only the element  $\mathbf{Z}_{22} \otimes \mathbf{z}(s)$ , which is equal to the inverse matrix of  $\mathbf{B}_{22} \otimes \mathbf{y}(s) - (\mathbf{B}_{21} \otimes \mathbf{y}(s))(\mathbf{B}_{11} \otimes \mathbf{y}(s))^{-1} (\mathbf{B}_{12} \otimes \mathbf{y}(s))$ . The proof process is detailed in Supplementary Material D.

Hence, the physical meaning of grid strength index calculation in dominant oscillation modes of heterogeneous synchronization control has been clarified through grid topology transformation.

#### D. Modified gSCR Calculation Method Considering GFM Converter

In the multi-infeed system of GFL converter,  $SCR_{\text{GFL}}$  is defined as the minimum eigenvalue of the extended admittance matrix, corresponding to the sub-synchronization oscillation mode in the weak grid [13]:

$$SCR_{\text{GFL}} = \lambda_{\min}(\mathbf{S}^{-1} \mathbf{B}_{\text{multi}}) \quad (20)$$

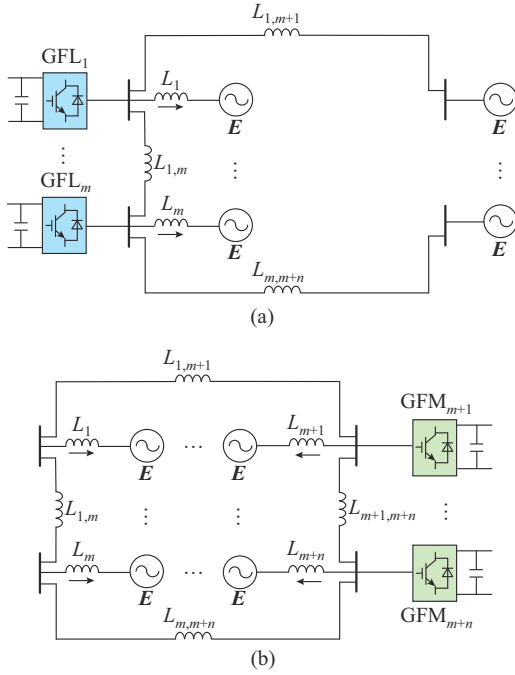


Fig. 10. Schematic diagram of equivalent circuit in different dominant oscillation modes. (a) GFL-dominated oscillation mode. (b) GFM-dominated oscillation mode.

where  $\mathbf{S}$  is a diagonal matrix, the diagonal elements of which are the rated capacities of each GFL converter; and  $\lambda_{\min}(\cdot)$  is the minimum eigenvalue of the solution matrix.

Reference [32] proposes a gSCR calculation method based on SDP according to (20). In order to consider the influence of the GFM converter, the SDP model in [32] can be improved as:

$$\begin{cases} \max \lambda_{\min} \\ \text{s.t. } \lambda_{\min} \mathbf{S}_{\text{GFL}} \leq \mathbf{B}_{11} \end{cases} \quad (21)$$

where  $\mathbf{S}_{\text{GFL}}$  is the diagonal matrix representing the GFL converter capacity.

The validity of (21) is explained by the following two parts:

1) Through the analysis in Section III-B, it can be observed that when facing the sub-synchronization oscillation mode dominated by PLL, the GFM converter is equivalent to a short circuit.

2) The inequality constraints of (21) are equivalent to the gSCR SDP form in [32].

Furthermore, based on the modeling and analysis in [13], the grid strength of the multi-infeed system of GFM converter  $SCR_{\text{GFM}}$  is defined as the maximum eigenvalue of the extended admittance matrix, corresponding to the low-frequency oscillation mode in stiff grid, as shown in (22), which has an SDP constraint form similar to (21).

$$SCR_{\text{GFM}} = \lambda_{\max}(\mathbf{S}^{-1} \mathbf{B}) \quad (22)$$

where  $\lambda_{\max}(\cdot)$  is the maximum eigenvalue of the solution matrix.

Further considering the influence of the GFL converter, combined with the open-circuit approximation of the GFL converter in Section III-C, the improved SDP model can be obtained as:

$$\begin{cases} \min \lambda_{\max} \\ \text{s.t. } \lambda_{\max} \mathbf{S}_{\text{GFM}} \geq \mathbf{B}_{22} - \mathbf{B}_{21} \mathbf{B}_{11}^{-1} \mathbf{B}_{12} \end{cases} \quad (23)$$

where  $\mathbf{S}_{\text{GFM}}$  is the diagonal matrix representing the GFM converter capacity.

#### IV. MODIFIED GSCR APPLICATION

The site selection of wind farms hinges on the availability of local natural resources. In areas with stiff grid, GFL converters are primarily selected, which can reduce the oscillation risk. In areas with weak grid, GFM converters are primarily selected. However, considering the inadequate transient stability of GFM converters in weak grid [7], when planning the maximum installed capacity of renewable energy equipment, it is imperative to minimize the allocation capacity of GFM converters while meeting the constraints of grid strength. Based on the calculation method of the modified gSCR considering GFM converters, if the CSCR of the GFL converter  $CSCR_{\text{GFL}}$  and the CSCR of the GFM converter  $CSCR_{\text{GFM}}$  are known ( $CSCR_{\text{GFL}}$  is less than  $CSCR_{\text{GFM}}$ ), the planning of the maximum installed capacity of renewable energy equipment can be used as the objective function for renewable energy capacity configuration.

$$\begin{cases} \max (\sum \mathbf{S}_{\text{GFL}} - \sum \mathbf{S}_{\text{GFM}}) \\ \text{s.t. } \lambda_{\min} \geq CSCR_{\text{GFL}} \\ \lambda_{\min} \mathbf{S}_{\text{GFL}} \leq \mathbf{B}_{11} \\ \lambda_{\max} \leq CSCR_{\text{GFM}} \\ \lambda_{\max} \mathbf{S}_{\text{GFM}} \geq (\mathbf{B}_{22} - \mathbf{B}_{21} \mathbf{B}_{11}^{-1} \mathbf{B}_{12}) \end{cases} \quad (24)$$

$$\begin{bmatrix} \mathbf{S}_{\text{GFL}} & \\ & \mathbf{S}_{\text{GFM}} \end{bmatrix} \leq \begin{bmatrix} \mathbf{B}_{11} & \mathbf{B}_{12} \\ \mathbf{B}_{21} & \mathbf{B}_{22} \end{bmatrix} \quad (25)$$

Since constraint (24) is a bilinear problem, it is difficult to solve. Therefore, let  $\delta_1 = 1/\lambda_{\min}$ ,  $\delta_2 = 1/\lambda_{\max}$ , then the bilinear problem can be converted into a semidefinite programming problem as shown in (26).

$$\begin{cases} \delta_1 \cdot CSCR_{\text{GFL}} \leq 1 \\ \mathbf{S}_{\text{GFL}} \leq \delta_1 \mathbf{B}_{11} \\ \delta_2 \cdot CSCR_{\text{GFM}} \geq 1 \\ \mathbf{S}_{\text{GFM}} \geq \delta_2 (\mathbf{B}_{22} - \mathbf{B}_{21} \mathbf{B}_{11}^{-1} \mathbf{B}_{12}) \end{cases} \quad (26)$$

Constraint (26) represents that the system satisfies the grid strength constraints that neither subsynchronization oscillation nor low-frequency oscillation occurs. Constraint (25) is a static voltage stability constraint, i.e., the gSCR of a single-infeed system is greater than 1.

#### V. SIMULATION RESULTS

This section first builds a hybrid system through the MATLAB/Simulink platform for time-domain simulation to verify the sub-synchronization and low-frequency oscillations caused by different synchronization control links under different grid strengths. Secondly, a 4-converter integrated system is built to verify the proposed method. Finally, a numerical analysis is performed on the SDP model to illustrate the engineering significance of the optimization results.

### A. Verification of Reduced-order Hybrid System

Taking the parameters of different grid strengths shown in Fig. 6 as a reference, the heterogeneous synchronization control parameters of the hybrid system are adjusted, as shown in Fig. 9, thereby stimulating the system to produce sub-synchronization and low-frequency oscillations. At the same time, the effectiveness of the reduced-order circuit is verified by comparing the SCR of the reduced-order model in different dominant oscillation modes with the CSCR of the single-feed system.

According to the proposed method, the node admittance matrices of the hybrid system under sub-synchronization oscillation and low-frequency oscillation, i. e.,  $\mathbf{B}_{\text{SSO}}$  and  $\mathbf{B}_{\text{LFO}}$  can be set as:

$$\begin{cases} \mathbf{B}_{\text{SSO}} = \begin{bmatrix} 1.73 & -2 \\ -2 & 13.5 \end{bmatrix} \\ \mathbf{B}_{\text{LFO}} = \begin{bmatrix} 3 & -2 \\ -2 & 11.5 \end{bmatrix} \end{cases} \quad (27)$$

At this time,  $\lambda_{\min} = 1.75$  and  $\lambda_{\max} = 13$ . When  $t = 0$  s, the PLL integral coefficient  $K_{\text{iPLL}}$  changes from the initial stable value 4000 to 6000. Sub-synchronization oscillation caused by the PLL dominant control link occurs in the hybrid system, with a frequency of about 11.5 Hz. The output power of the converter under sub-synchronization oscillation is shown in Fig. 11(a). Similarly, starting from the stable initial value at  $t = 0$  s, the damping parameter  $D$  changes from 46 to 26, and the system produces low-frequency oscillation dominated by virtual synchronization control, with an oscillation frequency of about 2.6 Hz. The output power of the converter under low-frequency oscillation is shown in Fig. 11(b).

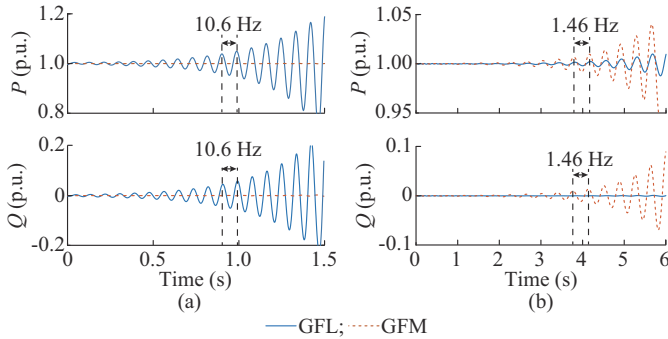


Fig. 11. Output power of converter under different oscillations. (a) Under sub-synchronization oscillation. (b) Under low-frequency oscillation.

It is worth noting that although a larger line mutual inductance is set in (27), the GFL converter in the hybrid system is still slightly affected by the low-frequency oscillation of the GFM converter. This is because the GFL converter undergoes forced oscillation. The specific analysis will be given through the participation factor calculation in Section V-B.

### B. Verification of Modified gSCR Calculation Method Considering GFM Converter

A 4-converter integrated system is constructed on the MATLAB/Simulink platform, as shown in Fig. 12, in which

Bus 1 and 2 are connected to GFL converters, and Bus 3 and 4 are connected to GFM converters. The control parameters of the GFL and GFM converters used in the system are shown in Supplementary Material A.

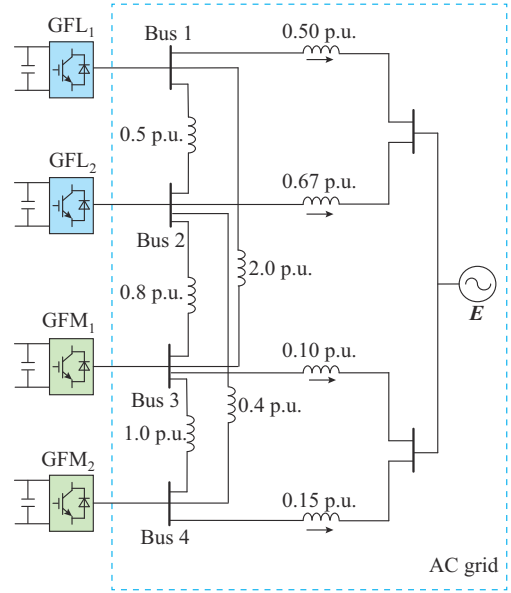


Fig. 12. A 4-converter integrated system.

First, the capacity of the converters on the four buses is set to be 1 p.u..  $\text{SCR}_{\text{GFM}}$  is calculated as 9.14 through (23), and the system undergoes low-frequency oscillation. Subsequently, when  $t = 3$  s, the GFM converter capacity increases to 2 p.u.. At this time, the  $\text{SCR}_{\text{GFM}}$  is reduced to 4.57, and the system is stable. The simulation results of the 4-converter integrated system are shown in Fig. 13.

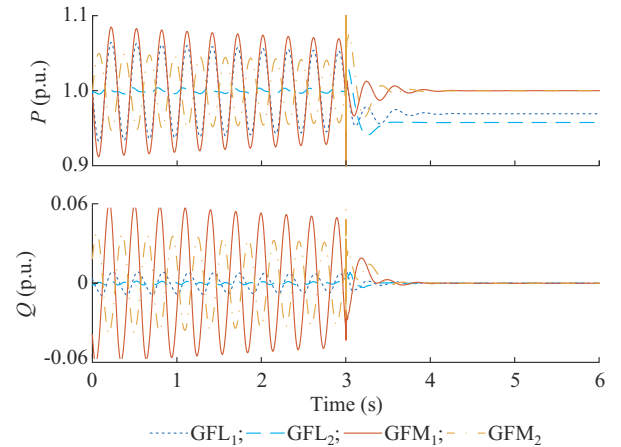


Fig. 13. Simulation results of 4-converter integrated system.

It can be observed that the GFL converter is affected by the low-frequency oscillation of the GFM converter to a certain extent. Therefore, this subsection calculates the participation factor of the dominant eigenvalue shown in Table II. The pole-zero map of the 4-converter integrated system at the equilibrium point is shown in Fig. 14, where  $\circ$  represents zeros, and  $\times$  represents poles.

TABLE II  
PARTICIPATION FACTOR CALCULATION OF DOMINANT EIGENVALUES

State variable	Dominant eigenvalue under sub-synchronization oscillation ( $-3.521 \pm 67.128i$ )	Dominant eigenvalue under low-frequency oscillation ( $-1.497 \pm 20.048i$ )
$\theta$ for GFM <sub>1</sub>	0.000126	0.428700
$\omega$ for GFM <sub>1</sub>	0.000134	0.259400
$\theta$ for GFM <sub>2</sub>	0.000173	0.037200
$\omega$ for GFM <sub>2</sub>	0.000184	0.022500
$\theta$ for GFL <sub>1</sub>	0.517900	0.000850
$\omega$ for GFL <sub>1</sub>	0.481600	0.000845
$\theta$ for GFL <sub>2</sub>	0.018600	0.000854
$\omega$ for GFL <sub>2</sub>	0.017600	0.000849

Note: state variables are two integrators in synchronization control link of four converters.

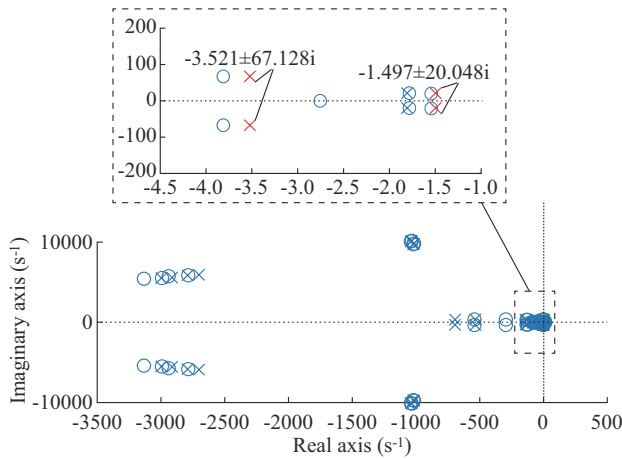


Fig. 14. Pole-zero map of 4-converter integrated system.

### C. Verification of Modified gSCR Application

The `sdpt3` solver in the optimization toolbox YALMIP in MATLAB is used to solve the capacity planning problem in Section IV. Figure 15 shows the capacity configuration of renewable energy equipment for the 4-converter integrated system. In addition, Fig. 16 provides the simulation results of the converter capacity configuration, where the voltage disturbance of 0.1 p.u. lasts for 0.1 s. The control parameters are the same as those in Fig. 12. At 1 s, the system experiences a 0.1 p.u. voltage disturbance at Bus 3, as shown in Fig. 12, which lasts for 0.1 s. During this process, the system remains stable, proving the feasibility of this optimization scheme.

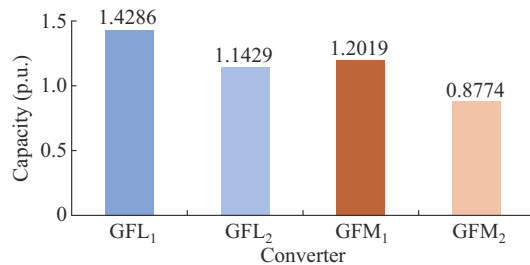


Fig. 15. Capacity configuration of renewable energy equipment.

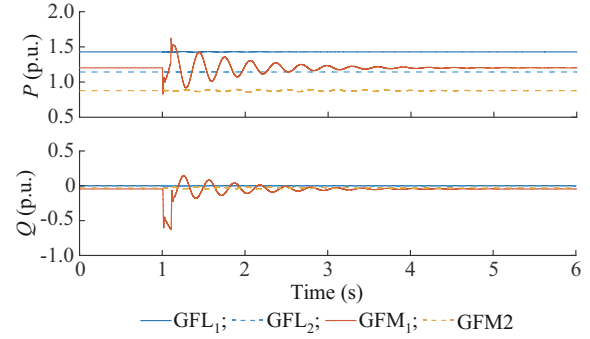


Fig. 16. Simulation results of converter capacity configuration.

## VI. CONCLUSION

This paper presents a grid strength assessment method for evaluating the small-signal stability of hybrid systems. The method incorporates sub-synchronization oscillation risk, primarily governed by the PLL, and low-frequency oscillation risk, influenced by virtual synchronization control, within grid planning applications. An SDP model is introduced, integrating the node admittance matrix and the capacity of grid-connected equipment. Simulation and numerical analysis results validate the effectiveness of the proposed method. In future work, we aim to further integrate transient stability and oscillation modes dominated by other control loops to deeply analyze the stability constraints that restrict the integration capacity of the GFM converter.

## REFERENCES

- [1] B. Kroposki, B. Johnson, Y. Zhang *et al.*, "Achieving a 100% renewable grid: operating electric power systems with extremely high levels of variable renewable energy," *IEEE Power and Energy Magazine*, vol. 15, no. 2, pp. 61-73, Mar. 2017.
- [2] F. Milano, F. Dörfler, G. Hug *et al.*, "Foundations and challenges of low-inertia systems," in *Proceedings of 2018 Power Systems Computation Conference (PSCC)*, Dublin, Ireland, Jun. 2018, pp. 1-25.
- [3] N. Hatziaargyriou, J. Milanovic, C. Rahmann *et al.*, "Definition and classification of power system stability – revisited & extended," *IEEE Transactions on Power Systems*, vol. 36, no. 4, pp. 3271-3281, Jul. 2021.
- [4] W. Du, W. Dong, and H. Wang, "A method of reduced-order modal computation for planning grid connection of a large-scale wind farm," *IEEE Transactions on Sustainable Energy*, vol. 11, no. 3, pp. 1185-1198, Jul. 2020.
- [5] B. Wen, D. Dong, D. Boroyevich *et al.*, "Impedance-based analysis of grid-synchronization stability for three-phase paralleled converters," *IEEE Transactions on Power Electronics*, vol. 31, no. 1, pp. 26-38, Jan. 2016.
- [6] X. Wang and F. Blaabjerg, "Harmonic stability in power electronic-based power systems: concept, modeling, and analysis," *IEEE Transactions on Smart Grid*, vol. 10, no. 3, pp. 2858-2870, May 2019.
- [7] X. Wang, M. G. Taul, H. Wu *et al.*, "Grid-synchronization stability of converter-based resources – an overview," *IEEE Open Journal of Industry Applications*, vol. 1, pp. 115-134, Aug. 2020.
- [8] J. Liu, W. Yao, J. Wen *et al.*, "Impact of power grid strength and PLL parameters on stability of grid-connected DFIG wind farm," *IEEE Transactions on Sustainable Energy*, vol. 11, no. 1, pp. 545-557, Jan. 2020.
- [9] M. Osman, N. Segal, A. Najafzadeh *et al.* (2018, Feb.). Short-circuit modeling and system strength white paper. [Online]. Available: [https://www.nerc.com/pa/RAPA/ra/Reliability%20Assessments%20DL/Short\\_Circuit\\_whitepaper\\_Final\\_1\\_26\\_18.pdf](https://www.nerc.com/pa/RAPA/ra/Reliability%20Assessments%20DL/Short_Circuit_whitepaper_Final_1_26_18.pdf)
- [10] Y. Zhang, S. Huang, J. Schmall *et al.*, "Evaluating system strength for large-scale wind plant integration," in *Proceedings of 2014 IEEE PES General Meeting Conference & Exposition*, National Harbor, USA, Jul. 2014, pp. 1-5.

- [11] P. F. D. Toledo, B. Bergdahl, and G. Asplund, "Multiple infeed short circuit ratio-aspects related to multiple HVDC into one AC network," in *Proceedings of 2005 IEEE/PES Transmission & Distribution Conference & Exposition: Asia and Pacific*, Dalian, China, Aug. 2005, pp. 1-6.
- [12] F. Zhang, H. Xin, D. Wu *et al.*, "Assessing strength of multi-infeed LCC-HVDC systems using generalized short-circuit ratio," *IEEE Transactions on Power Systems*, vol. 34, no. 1, pp. 467-480, Jan. 2019.
- [13] W. Dong, H. Xin, D. Wu *et al.*, "Small signal stability analysis of multi-infeed power electronic systems based on grid strength assessment," *IEEE Transactions on Power Systems*, vol. 34, no. 2, pp. 1393-1403, Jan. 2019.
- [14] G. Wang, H. Xin, D. Wu *et al.*, "Grid strength assessment for inhomogeneous multi-infeed HVDC systems via generalized short circuit ratio," *Journal of Modern Power Systems and Clean Energy*, vol. 11, no. 4, pp. 1370-1374, Jul. 2023.
- [15] Q. Shi, G. Wang, L. Ding *et al.*, "A sufficient condition for small-signal synchronization stability with applications to PLL-dominated oscillation mode analysis," *International Journal of Electrical Power & Energy Systems*, vol. 157, p. 109882, Jun. 2024.
- [16] W. Du, Z. Chen, K. P. Schneider *et al.*, "A comparative study of two widely used grid-forming droop controls on microgrid small-signal stability," *IEEE Journal of Emerging and Selected Topics in Power Electronics*, vol. 8, no. 2, pp. 963-975, Jun. 2020.
- [17] D. Groß, M. Colombino, J.-S. Brouillon *et al.*, "The effect of transmission-line dynamics on grid-forming dispatchable virtual oscillator control," *IEEE Transactions on Control of Network Systems*, vol. 6, no. 3, pp. 1148-1160, Sept. 2019.
- [18] L. Huang, H. Xin, H. Yuan *et al.*, "Damping effect of virtual synchronous machines provided by a dynamical virtual impedance," *IEEE Transactions on Energy Conversion*, vol. 36, no. 1, pp. 570-573, Mar. 2021.
- [19] Y. Liao, X. Wang, F. Liu *et al.*, "Sub-synchronous control interaction in grid-forming VSCs with droop control," in *Proceedings of 2019 4th IEEE Workshop on the Electronic Grid (eGRID)*, Xiamen, China, Nov. 2019, pp. 1-6.
- [20] S. Wang, Z. Liu, J. Liu *et al.*, "Small-signal modeling and stability prediction of parallel droop-controlled inverters based on terminal characteristics of individual inverters," *IEEE Transactions on Power Electronics*, vol. 35, no. 1, pp. 1045-1063, Jan. 2020.
- [21] R. H. Lasseter, Z. Chen, and D. Pattabiraman, "Grid-forming inverters: a critical asset for the power grid," *IEEE Journal of Emerging and Selected Topics in Power Electronics*, vol. 8, no. 2, pp. 925-935, Jun. 2020.
- [22] Y.-K. Kim, G.-S. Lee, J.-S. Yoon *et al.*, "Evaluation for maximum allowable capacity of renewable energy source considering AC system strength measures," *IEEE Transactions on Sustainable Energy*, vol. 13, no. 2, pp. 1123-1134, Apr. 2022.
- [23] C. Yang, L. Huang, H. Xin *et al.*, "Placing grid-forming converters to enhance small signal stability of PLL-integrated power systems," *IEEE Transactions on Power Systems*, vol. 36, no. 4, pp. 3563-3573, Jul. 2021.
- [24] Y. Zhou, H. Xin, D. Wu *et al.*, "Small-signal stability assessment of heterogeneous grid-following converter power systems based on grid strength analysis," *IEEE Transactions on Power Systems*, vol. 38, no. 3, pp. 2566-2579, May 2023.
- [25] Y. Li, Y. Gu, and T. C. Green, "Revisiting grid-forming and grid-following inverters: a duality theory," *IEEE Transactions on Power Systems*, vol. 37, no. 6, pp. 4541-4554, Nov. 2022.
- [26] Y. Li, Y. Gu, Y. Zhu *et al.*, "Impedance circuit model of grid-forming inverter: visualizing control algorithms as circuit elements," *IEEE Transactions on Power Electronics*, vol. 36, no. 3, pp. 3377-3395, Mar. 2021.
- [27] B. Wen, D. Boroyevich, R. Burgos *et al.*, "Analysis of D-Q small-signal impedance of grid-tied inverters," *IEEE Transactions on Power Electronics*, vol. 31, no. 1, pp. 675-687, Jan. 2016.
- [28] L. Huang, H. Xin, W. Dong *et al.* (2022, Aug.). Impacts of grid structure on PLL-synchronization stability of converter-integrated power systems. [Online]. Available: <https://doi.org/10.1016/j.ifacol.2022.07.270>
- [29] L. Harnefors, F. M. M. Rahman, M. Hinkkanen *et al.*, "Reference-feedforward power-synchronization control," *IEEE Transactions on Power Electronics*, vol. 35, no. 9, pp. 8878-8881, Sept. 2020.
- [30] X. Wang, Y. Song, and M. Irving, *Modern Power Systems Analysis*. Berlin: Springer Science & Business Media, 2010.
- [31] H. Liu, X. Xie, J. He *et al.*, "Subsynchronous interaction between direct-drive PMSG based wind farms and weak AC networks," *IEEE Transactions on Power Systems*, vol. 32, no. 6, pp. 4708-4720, Nov. 2017.
- [32] H. Yuan, H. Xin, D. Wu *et al.*, "Assessing maximal capacity of grid-following converters with grid strength constraints," *IEEE Transactions on Sustainable Energy*, vol. 13, no. 4, pp. 2119-2132, Oct. 2022.

**Qianhong Shi** received the M.S. degree in electrical power system engineering from the University of Manchester, Manchester, UK, in 2018. She is currently pursuing the Ph.D. degree in the Department of Electrical Engineering, Shandong University, Jinan, China. Her research interests include small-signal stability analysis of renewable energy integrated power systems.

**Wei Dong** received the B.S. and Ph.D. degrees in electrical engineering from the School of Electrical Engineering, Zhejiang University, Hangzhou, China, in 2014 and 2019, respectively. He is currently working in the Electric Power Research Institute, State Grid Zhejiang Electric Power Co., Ltd., Hangzhou, China. His research interests include renewable energy stability analysis and control.

**Guanzhong Wang** received the B.Eng. and Ph.D. degrees in electrical engineering from Zhejiang University, Hangzhou, China, in 2013 and 2019, respectively. He is currently working as an Associate Researcher with the Department of Electrical Engineering, Shandong University, Jinan, China. His research interests include stability analysis of high-voltage direct current and renewable energy integrated power systems.

**Junchao Ma** received the B.S. and Ph.D. degrees in electrical engineering from the College of Electrical Engineering, Zhejiang University, Hangzhou, China, in 2012 and 2017, respectively. He is currently working in the Electric Power Research Institute, State Grid Zhejiang Electric Power Co., Ltd., Hangzhou, China. His research interests include energy management of medium-voltage direct current systems and power system operation.

**Chenxu Wang** received the Ph.D. degree in electrical engineering from the School of Electrical Engineering and Automation, Wuhan University, Wuhan, China, in 2021. He is currently working in the Electric Power Research Institute, State Grid Zhejiang Electric Power Co., Ltd., Hangzhou, China. His research interests include renewable energy stability analysis and control.

**Xianye Guo** received the B.S. degree in the Department of Electrical Engineering, Shandong University, Jinan, China, in 2024. He is currently pursuing the M.S. degree in the Department of Electrical Engineering, Shandong University. His research interests include vector control, synchronous control, and their interaction with power grid.

**Vladimir Terzija** received the Dipl.-Ing., M.Sc., and Ph.D. degrees in electrical engineering from the University of Belgrade, Belgrade, Serbia, in 1988, 1993, and 1997, respectively. He is currently a Professor of energy systems and networks with the Newcastle University, Newcastle upon Tyne, UK. He is also a Distinguished Visiting Professor with Shandong University, Jinan, China, and a Guest Professor with the Technical University of Munich, Munich, Germany. During 2021-2023, he was a Full Professor with Skolkovo Institute of Science and Technology, Moscow, Russian Federation. During 2006-2020, he was the EPSRC Chair Professor with The University of Manchester, Manchester, UK. From 2000 to 2006, he was a Senior Specialist for switchgear and distribution automation with ABB, Ratingen, Germany. From 1997 to 1999, he was an Associate Professor with the University of Belgrade, Belgrade, Serbia. He is the Editor-in-Chief of International Journal of Electrical Power and Energy Systems, Humboldt Fellow and the recipient of the National Friendship Award, China. His current research interests include smart grid application, wide-area monitoring, protection and control, multi-energy system, transient process, information and communication technology, data analytics, and complex science application in power systems.